RESEARCH ARTICLE

Editor's Choice

ADVANCED MATERIALS INTERFACES

www.advmatinterfaces.de

Glycosylated MoS_2 Sheets for Capturing and Deactivating *E. coli* Bacteria: Combined Effects of Multivalent Binding and Sheet Size

Shaohui Xu, Sumati Bhatia, Xin Fan, Philip Nickl, and Rainer Haag**

Molybdenum disulfide (MoS_2) holds great promise for antibacterial applications owing to its strong photothermal performance and biocompatibility. Most of its antibacterial explorations have sought enhanced antibacterial potency through designing new hybrid inorganic materials, the relationship between its physiochemical properties and antibacterial activities has yet to be explored. This work is the first to investigate the combination effects of different sized and functionalized MoS_2 sheets on their antibacterial activities. The bacterial capture abilities of 3 μm mannosylated, galactosylated, and glucosylated sheets, as well as 300 nm mannosylated sheets, all with similar sugar densities, are compared. Only mannosylated MoS_2 sheets are found to agglutinate normal *Escherichia coli* (*E. coli*) and large mannosylated MoS_2 sheets show the strongest *E. coli* agglutination. Despite slightly weaker photothermal performance under near-infrared (NIR) laser irradiation, large mannosylated MoS_2 sheets exhibit higher antibacterial activity than the smaller sheets. By much stronger specific multivalent binding, large sheets capture *E. coli* more efficiently and compensate for their reduced photothermal activity. Besides providing a facile approach to eliminate *E. coli* bacteria, these findings offer valuable guidance for future development of 2D nanomaterial-based antibacterial agents and filter holder materials, where large-functionalized sheets can capture and eliminate bacteria powerfully.

1. Introduction

Bacterial infections rank among the major threats to global health, especially for hospitalized and immunocompromised patients.[1,2] As the most common initiator of urinary tract infections, *Escherichia coli (E. coli)* bacteria kill high numbers of newborns in underdeveloped countries.[3,4] Antibiotics have been the most effective therapeutics for several decades, and their discovery and development have greatly extended the average human lifespan. Antibiotic resistance occurs naturally, however, the misuse of antibiotics has now accelerated this process and presented it as a major threat to global heath, food security, and drinking water safety.[2] Hence, novel alternative antimicrobials are urgently needed to address this increasing concern.

With the rapid development of nanotechnology, novel nanomaterials developed by researchers offer various anti-infective strategies to combat bacterial infections, such as targeted antibiotic therapy, photothermal therapy (PTT), and photodynamic therapy (PDT).[5,6] Especially, 2D materials, such as graphene, black phosphorus, MXenes, and transitional metal dichalcogenides (TMDs) are currently being explored extensively in biomedicine, since they have ultrathin structures, high specific surface areas, and unique physicochemical characteristics, which are suitable for fabricating multivalent interaction.[7] MoS_2 in particular shows high photothermal conversion efficiency, low toxicity, and excellent biodegradability.[8] These advantages make it superior to other 2D materials and endow it with great potential to be a photothermal transduction agent in PTT.[7,9–11]

Previous studies have shown that the physicochemical properties of nanomaterials, such as lateral dimension, morphology, surface charge, and functionalities, are crucial to their biological behaviors.[12–14] For example, Zhang et al. reported that larger and thicker black phosphorous has the higher cellular cytotoxicity, whereas smaller one only shows moderate toxicity.[15] Yang et al. and Chen et al. separately reported that the particulate size and surface chemistry of graphene oxide (GO) is critical to its biological behaviors, especially in vivo.[16,17] However, up to now, the published works on MoS_2 for antibacterial applications mainly pursue the enhanced microcidal activities of MoS_2 hybrid composites.[18–21] Few reports have investigated MoS_2 as a multivalent binding platform against bacteria, and the effects of MoS_2's lateral size on antibacterial activities remain to be studied.

Multivalent interactions on the cell surface are essential to cell signaling, recognition cascades, and viral and bacterial infection processes.[22,23] For example, *E. coli* bacteria have rodlike FimH, which can bind multivalently to mannosylated glycoproteins and facilitate the adhesion of *E. coli* to host cells.[24,25] Though multivalent inhibitors do not show strong bactericidal activity, large multivalent bacteria binders significantly

S. Xu, S. Bhatia, X. Fan, P. Nickl, R. Haag
Institut für Chemie und Biochemie
Freie Universität Berlin
Takustraße 3, 14195 Berlin, Germany
E-mail: sumati@zedat.fu-berlin.de; haag@chemie.fu-berlin.de

The ORCID identification number(s) for the author(s) of this article can be found under https://doi.org/10.1002/admi.202102315.

DOI: 10.1002/admi.202102315

reduce adhesion of bacteria to host cells, thus slowing the evolution of drug-resistant strains.[25] And if multivalent structures are immobilized on multifunctional platforms, especially those possessing photothermal and magnetic properties, bacterial capture by the platforms can facilitate the isolation, removal, and elimination of bacteria.

In the present study, we constructed "multivalent, glycosylation-functionalized, water-soluble 2D platforms" by anchoring isomeric-sugar-ligand-functionalized polyglycerol (hPG), in identical densities, onto MoS_2 sheets of different sizes (**Scheme 1**). By comparing the agglutination abilities of the mannosylated, glucosylated, and galactosylated MoS_2 sheets for *E. coli* in aqueous suspension, we selected the most potent mannosylated sheets for further investigation. Based on this screening, we then examined functionalized MoS_2 sheets with small size (≈300 nm) and large size (≈3 μm) for photothermal properties and agglutination abilities. We also visualized the multivalent interactions between *E. coli* and MoS_2 sheets by scanning electron microscope (SEM) and transmission electron microscope (TEM). We conducted further experiments on the antibacterial activity of mannosylated MoS_2 sheets of different sizes to investigate the relationship between sheet size and antibacterial activity. Moreover, under NIR irradiation, large-size mannosylated MoS_2 sheets displayed outstanding bactericidal activity (over 99.9% deactivation efficiency) at a low concentration (150 μg mL^{-1}).

2. Results and Discussion

2.1. Preparation of Glycosylated MoS_2 Sheets

While various natural monosaccharides have been discovered in living organisms, three endogenous hexoses (D-mannose, D-glucose, and D-galactose) are particularly abundant. In *E. coli*, they play essential roles as structural components, signal transduction molecules, and energy suppliers, especially during glycolysis for energy production.[26] In this work, after exfoliation, pristine MoS_2 (mixtures of large and small sheets, SEM image in Figure S1, Supporting Information) was separately functionalized biodegradable MoS_2 sheets with D-mannose, D-glucose, and D-galactose, with their high structural similarities, and then these sheets' interactions with *E. coli*. as well as their microcidal efficiencies were compared. We functionalized azide-modified hPG in a single step by click reaction of propargylated sugar pentaacetates and propargylated lipoic acid (LA) residue to afford ≈40% sugar and 10% LA grafting (**Figure 1**a, Figures S2–S11, Supporting Information). The hydrolysis of pentaacetyl groups then afforded glycosylated and LA-conjugated hPG (see NMR analysis in Figure S2a and IR spectra in Figure S12, Supporting Information), which were installed on the exfoliated MoS_2 sheets by Mo—S bonds according to previous reported methods and then characterized by IR spectroscopy (Figures 1b, 2b).[27,28] Large $hPG(LA)_{10\%}$-functionalized MoS_2 sheets (without sugar functionalization, denoted as L-MoS_2-OH) were used as a control.

2.2. Characterizations of Glycosylated MoS_2 Sheets

First, the conjugation of mannosylated polyglycerols on MoS_2 sheets was confirmed by IR and thermogravimetric (TGA) analysis. The absorbance bands at 3336, 2873, and 1070 cm^{-1} were attributed to the stretching vibrations of the O—H, C—H, and C—O bonds in the polyglycerols (Figure 2b and Figure S12, Supporting Information). The peak at 3142 cm^{-1} was assigned to the characteristic peak

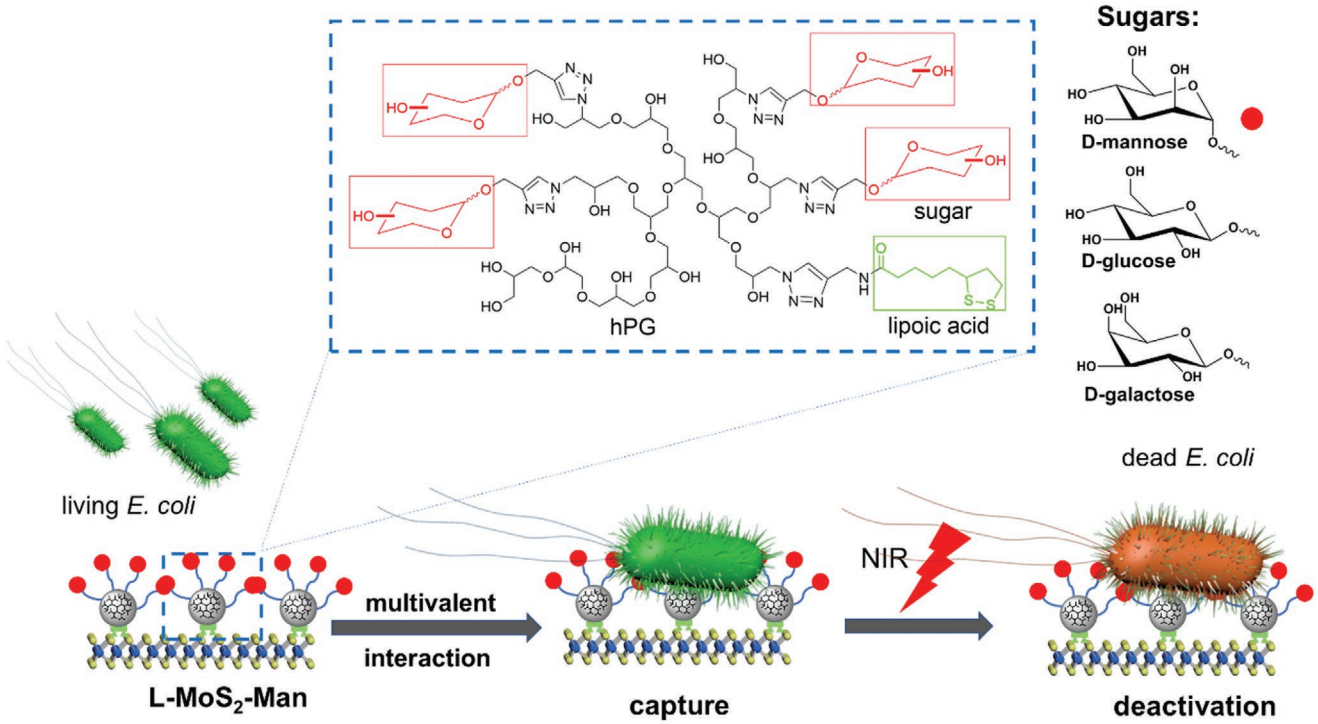

Scheme 1. Representation of glycosylated hPG-functionalized MoS_2 sheets and *E. coli* bacteria capture and deactivation by mannose functionalized MoS_2 sheets.

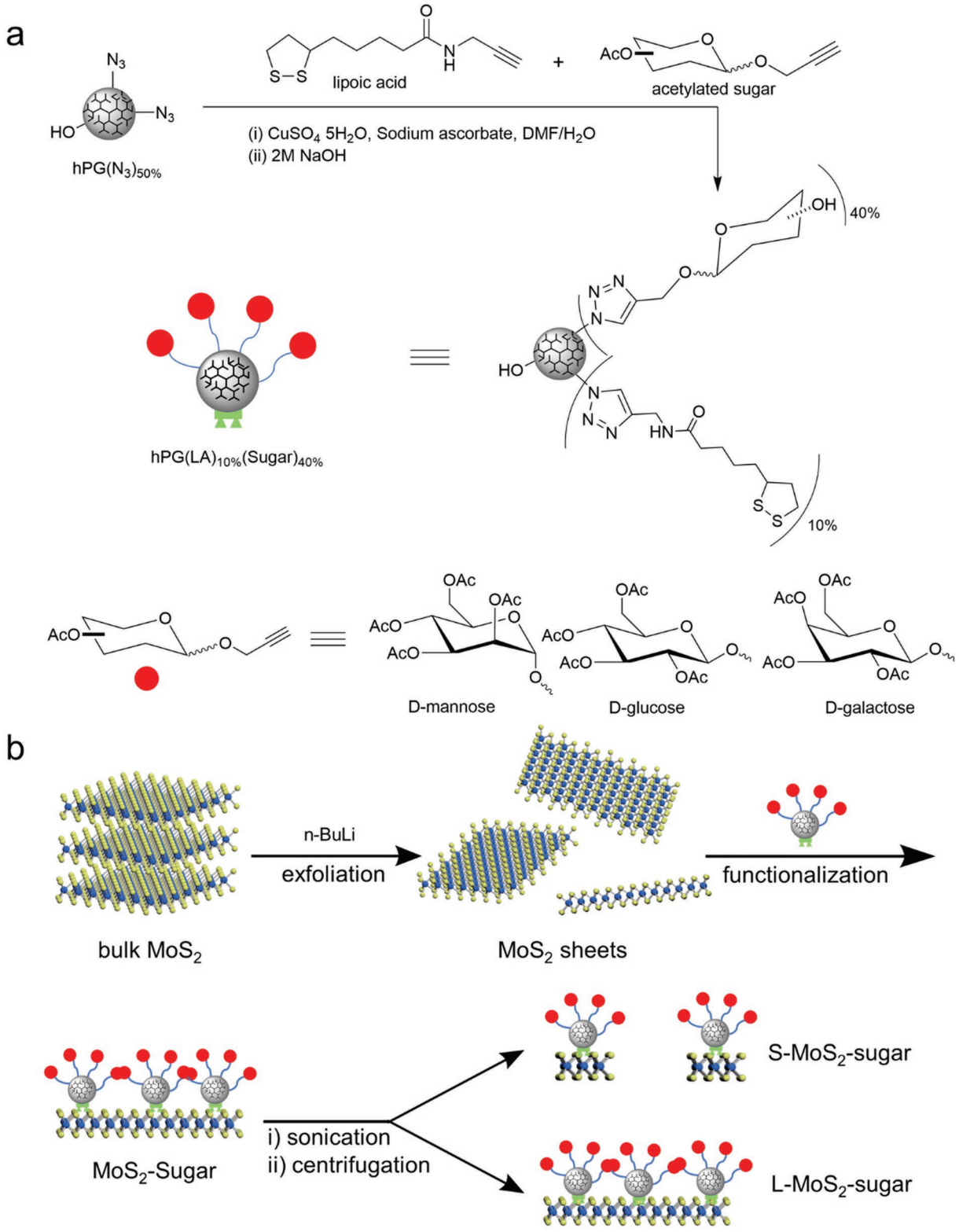

Figure 1. a) Synthesis of sugar-functionalized polyglycerols. b) Preparation of glycosylated MoS_2 sheets in large and small sizes.

of 1,2,3-triazole, while the region at 1650 cm^{-1} was attributed to the stretching vibration of the C=O bond in propargyl LA. These results confirmed the successful conjugation of glycosylated polyglycerol onto MoS_2 sheets. Furthermore, TGA profiles of mannosylated MoS_2 (MoS_2-Man) displayed a gradual decrease between 200 and 800 °C, from which

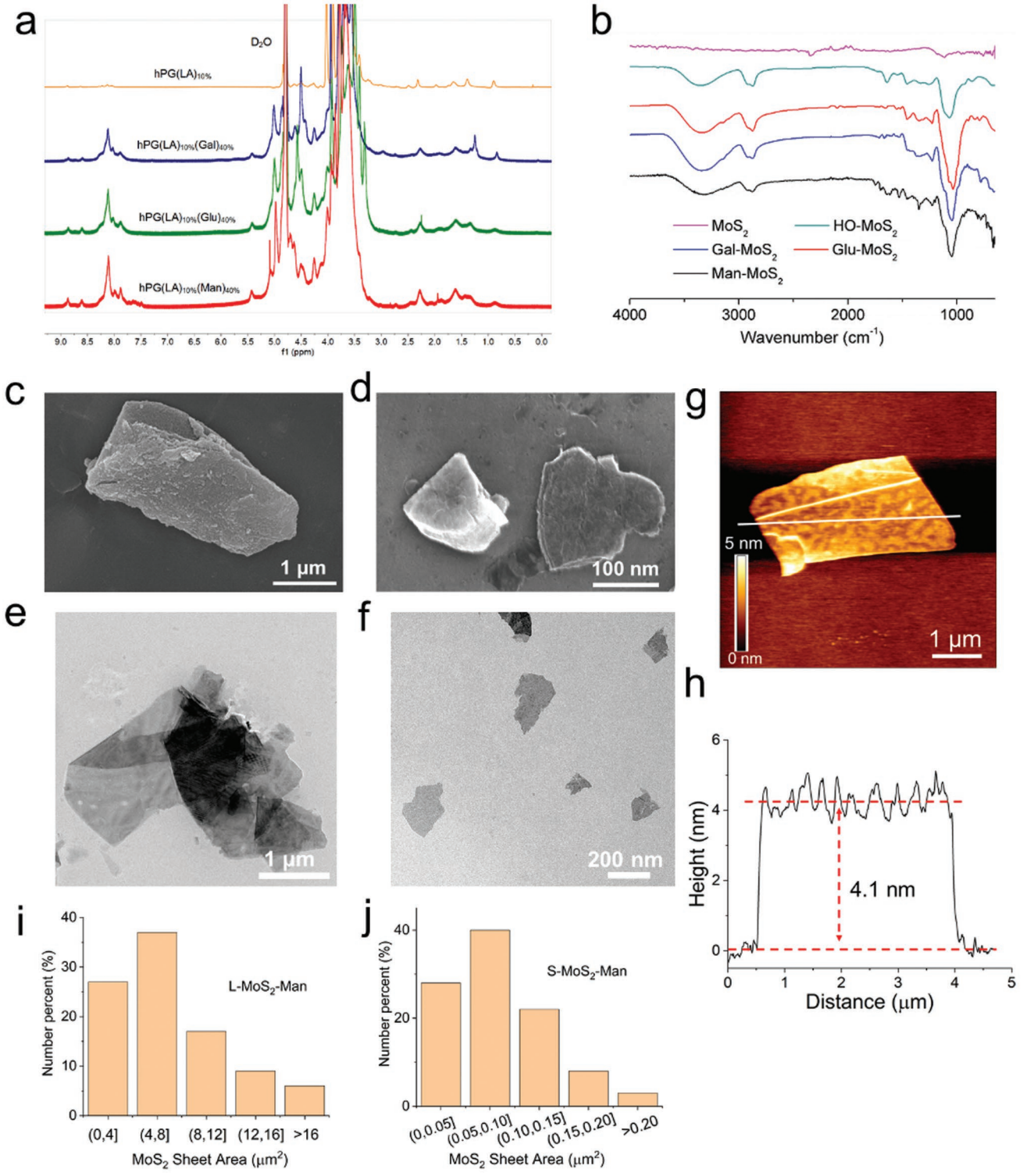

Figure 2. a) ^{1}H NMR spectra (600 MHz, D_2O) of $hPG(LA)_{10\%}(Man)_{40\%}$, $hPG(LA)_{10\%}(Glu)_{40\%}$, $hPG(LA)_{10\%}(Gal)_{40\%}$, and $hPG(LA)_{10\%}$. b) FTIR spectra of MoS_2-Man, MoS_2-Glu, MoS_2-Gal, MoS_2-OH, and pristine MoS_2. Representative SEM images of c) L-MoS_2-Man and d) S-MoS_2-Man. Representative TEM images of e) L-MoS_2-Man and f) S-MoS_2-Man. g) Representative AFM image of L-MoS_2-Man. h) Cross-section analysis of sheet height. Sheet area distributions of i) L-MoS_2-Man and j) S-MoS_2-Man as determined from SEM images (areas of 100 sheets were measured by Image J software).

the proportion of $hPG(LA)_{10\%}(Man)_{40\%}$ can be calculated as 20.1 wt. %, demonstrating a high degree of surface functionalization of $hPG(LA)_{10\%}(Man)_{40\%}$ on the MoS_2 sheets (**Figure 3**f).

In order to compare the physicochemical properties and capture abilities of large-size and small-size MoS_2 sheets, we prepared glycosylated MoS_2 sheets in large (≈3 μm) and small

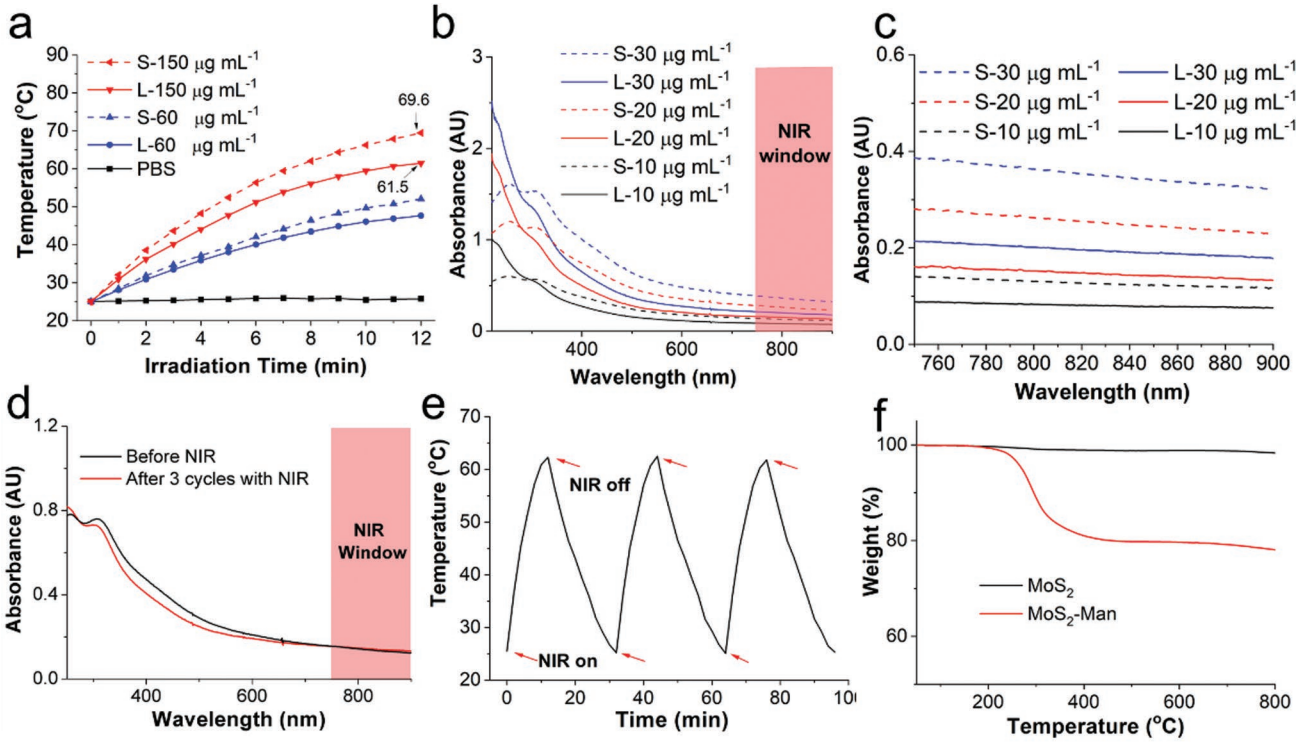

Figure 3. Characterizations: a) Temperatures of L-MoS_2-Man and S-MoS_2-Man aqueous solutions at 60 and 150 μg mL^{-1} under NIR irradiation. b) Ultraviolet-visible (UV–vis) spectra of L-MoS_2-Man and S-MoS_2-Man aqueous solutions at 10, 20, and 30 μg mL^{-1}. c) Absorbance in the NIR window of L-MoS_2-Man and S-MoS_2-Man aqueous solutions at 10, 20, and 30 μg mL^{-1}. d) UV–vis spectra of L-MoS_2-Man aqueous solution before and after 3 cycles of continuous NIR irradiation. e) Temperatures of L-MoS_2-Man aqueous solution during 3 cycles of continuous NIR irradiation (150 μg mL^{-1}). f) Thermal gravimetric analysis curves of pristine MoS_2 and MoS_2-Man under argon. The NIR irradiation (808 nm) at 1 W cm^{-2} was employed in all experiments.

(≈300 nm) sizes by controlling the sonication time periods, centrifugation speeds, and centrifugation time. Large and small mannosylated MoS_2 sheets are denoted respectively as L-MoS_2-Man and S-MoS_2-Man, and the other materials in this work are denoted in the same way. These abbreviations can be found in **Table 1** and Table S1, Supporting Information.MoS_2-Glu, MoS_2-Gal, and MoS_2-OH were also characterized by IR analysis (Figure 2b). SEM and TEM image (Figure 2c,e) showed that the prepared L-MoS_2-Man sheets were several layers thick, with a lateral size of around 3 μm. By contrast, the prepared S-MoS_2-Man sheets were only a few layers thick and had a lateral size of around 300 nm, according to the SEM (Figure 2d) and TEM (Figure 2f) analysis. The atomic force microscopy (AFM) imagery (Figure 2g,h) gave the lateral size of L-MoS_2-Man as ≈3 μm and its thickness as 4.1 nm. The respective average sheet areas of L-MoS_2-Man and S-MoS_2-Man were 7.45 and 0.09 μm^2, as determined from numerous SEM images. Sheet area distributions can be found in Figure 2i,j.

Table 1. Abbreviations of substances.

Abbreviations	Substances
hPG	hyperbranched polyglycerol
hPG-$(LA)_{10\%}$	hyperbranched polyglycerol with 10% lipoic acid groups
hPG-$(LA)_{10\%}(Man)_{40\%}$	deprotected mannose and lipoic acid functionalized PG
MoS_2-Man	mixture of large and small mannosylated MoS_2 sheets
MoS_2-Glu	mixture of large and small glucosylated MoS_2 sheets
MoS_2-Gal	mixture of large and small galactosylated MoS_2 sheets
MoS_2-OH	mixture of large and small non-glycosylated MoS_2 sheets (only hPG functionalization)
L-MoS_2-Man	large mannosylated MoS_2 sheets
S-MoS_2-Man	small mannosylated MoS_2 sheets
L-MoS_2-Glu	large glucosylated MoS_2 sheets
L-MoS_2-Gal	large galactosylated MoS_2 sheets
L-MoS_2-OH	large non-glycosylated MoS_2 sheets (only hPG functionalization)

It is reported that the NIR absorption and photothermal properties of MoS_2 sheets are closely related to their size.[29,30] As shown in Figure 3a, S-MoS_2-Man exhibited better photothermal performance than L-MoS_2-Man at the same concentration. Correspondingly, the absorbance of L-MoS_2-Man in the near-infrared (NIR) region of the spectrum is less than that of S-MoS_2-Man (Figure 3b,c). These results indicate that small sheets, with their higher specific surface areas and interface defects, more efficiently absorb NIR laser radiation and convert it into heat.[30] For example, the S-MoS_2-Man aqueous solution (150 μg mL^{-1}) showed the highest increase in temperature, rising to 69.6 °C, while the temperature of L-MoS_2-Man rose only to 61.5 °C at the same mass concentration. Moreover, L-MoS_2-Man sheets retained superior photothermal stability, as evidenced by the absence of obvious change in maximal

heating temperature in the same time period; colloidal stability; and absorbance in NIR region after three cycles of NIR irradiation (Figure 3d,e).

2.3. Agglutination Studies

The mannose-specific *E. coli* adhesin FimH of the type 1 pili binds with high affinity to mannose residues. Most *E. coli* bacterium types express FimH, while a few types do not express it and do not have a binding affinity to mannose residues. Many studies have demonstrated that multivalent architectures decorated with mannose epitopes can attract bacteria from ambient solutions and induce agglutination.[31–33] Here we investigated the specific binding ability of the three sugar moieties toward the FimH mannose-binding receptors on the *E. coli* bacteria surface by examining the binding of L-MoS_2-Man/Glu/Gal and L/S-MoS_2-Man to two *E. coli* strains, ORN 178 and ORN 208. The wild-type *E. coli* strain ORN 178 expresses FimH that can bind specifically to D-mannose. In contrast, the mutant *E. coli* strain ORN 208 does not express FimH and fails to bind to D-mannose. To monitor bacteria agglutination by confocal microscopy, both strains were stained with SYTO 9 after incubation with functionalized MoS_2 sheets. As shown in **Figure 4**a, we observed no aggregation in the L-MoS_2-OH group, indicating a lack of nonspecific interaction between polyglycerol and *E. coli*. Strong fluorescent clusters were formed in bacteria mixtures treated with L-MoS_2-Man, while no apparent aggregations were observed in the L-MoS_2-Glu and L-MoS_2-Gal groups (Figure 4b–d). These results further prove the selective binding of FimH with mannose residues. Not surprisingly, neither L-MoS_2-Man, L-MoS_2-Glu, nor L-MoS_2-Gal aggregated in ORN 208 suspensions, as ORN208 has no FimH receptor. Macroscopic observations further confirmed the confocal images' demonstrations

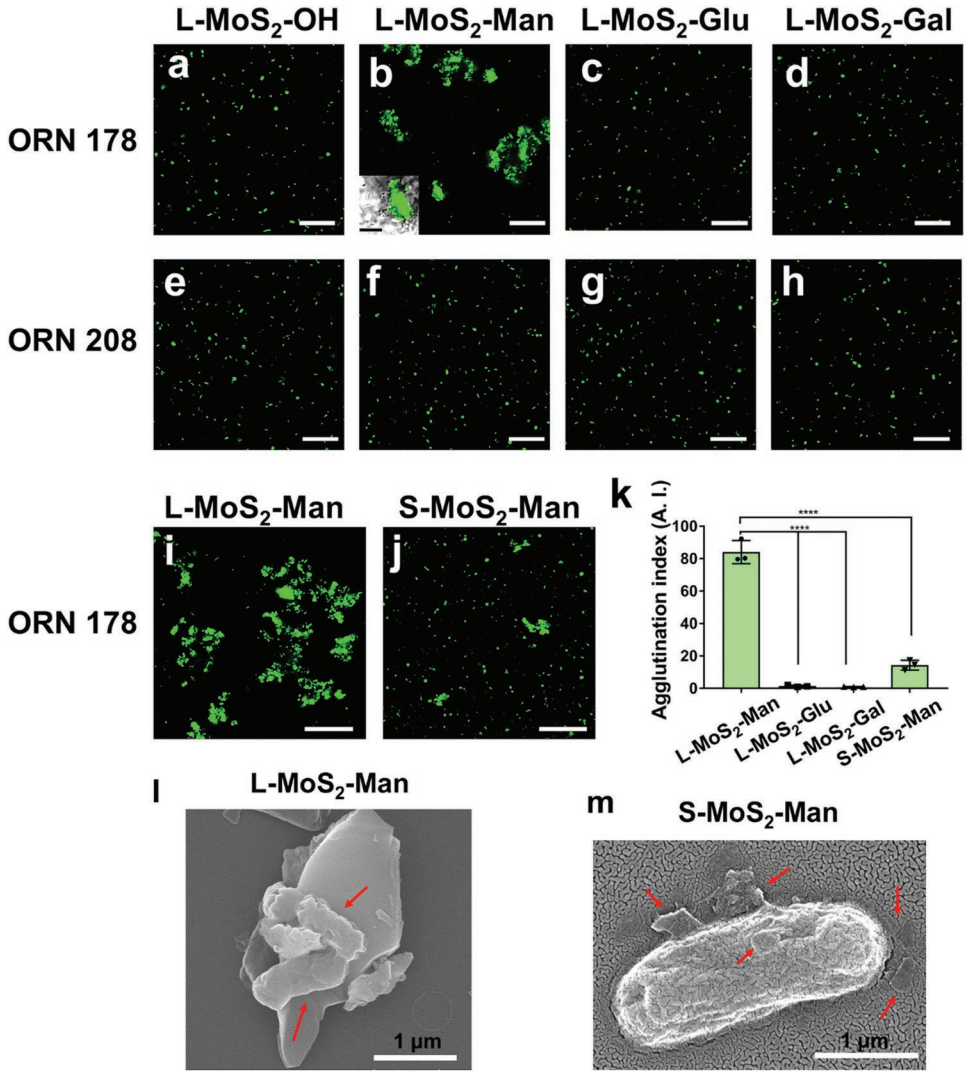

Figure 4. Agglutination studies of a) L-MoS_2-OH, b) L-MoS_2-Man, c) L-MoS_2-Glu, d) L-MoS_2-Gal, i) L-MoS_2-Man, and j) S-MoS_2-Man on *E. coli* strain ORN 178. Agglutination studies of e) L-MoS_2-OH, f) L-MoS_2-Man, g) L-MoS_2-Glu, and h) L-MoS_2-Gal on *E. coli* strain ORN 208. k) Quantitative results of agglutination indices from fluorescence images in Figure 4a–4j. Data are presented as mean ± SD, n = 3. Statistically significant differences are indicated by ****$p < 0.0001$. Scale bar: 20 µm. SEM images of interactions of *E. coli* ORN 178 bacteria with l) L-MoS_2-Man and m) S-MoS_2-Man.

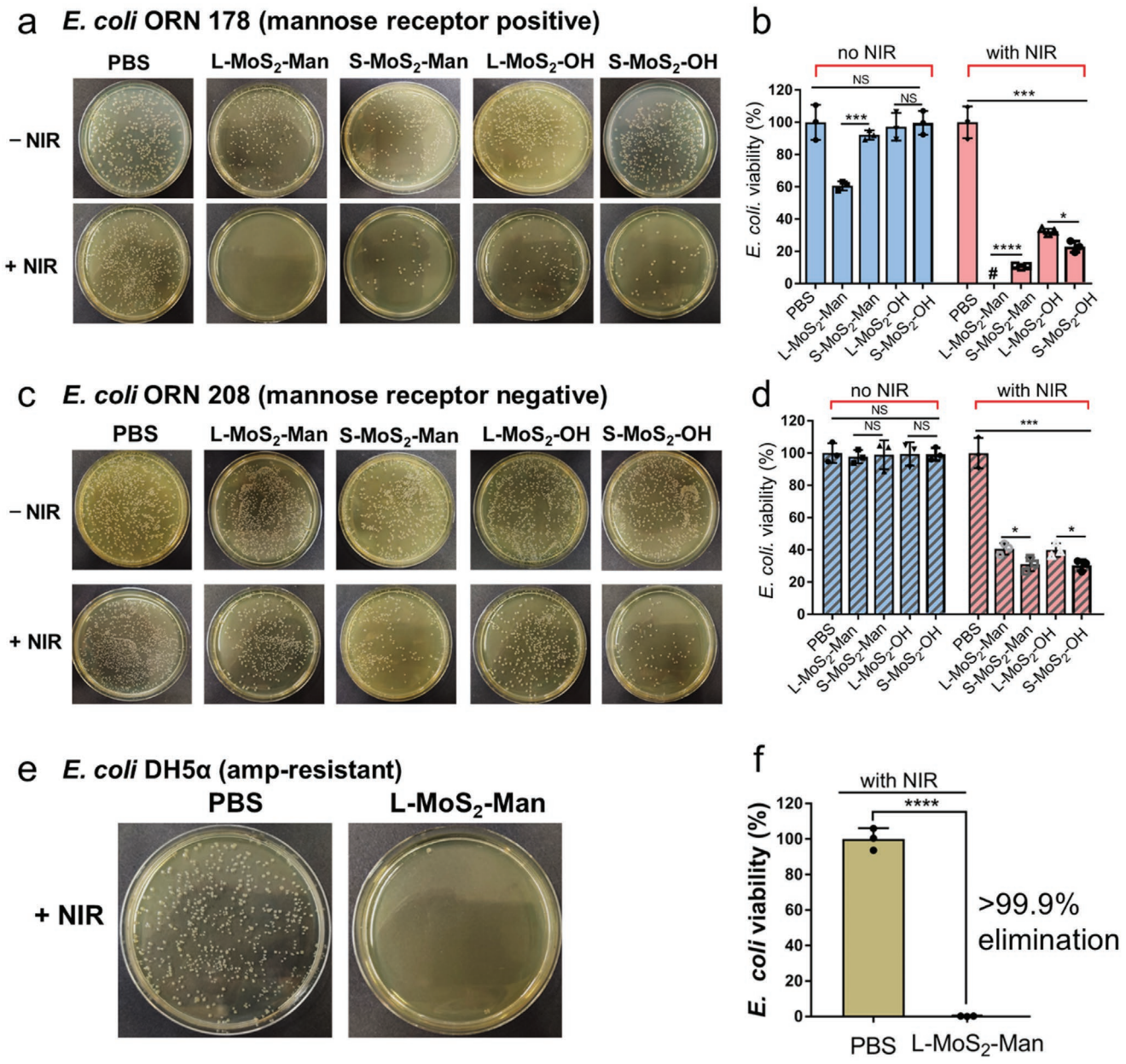

Figure 5. a) Typical photographs of *E. coli* strain ORN 178 colonies treated with PBS, L-MoS_2-Man, S-MoS_2-Man, L-MoS_2-OH, and S-MoS_2-OH, respectively (upper row: without NIR irradiation; lower row: with NIR irradiation). b) Quantification results of ORN 178 colonies after different treatments. c) Typical photographs of the colonies of *E. coli* strain ORN 208 treated with PBS, L-MoS_2-Man, S-MoS_2-Man, L-MoS_2-OH, and S-MoS_2-OH, respectively. d) Quantification results of ORN 208 colonies after different treatments. e) Typical photographs of the colonies for ampicillin-resistant *E. coli* strain DH5α treated with PBS and L-MoS_2-Man. Bacterial culture media with PBS treatment was used as the blank control for viability calculation. f) Quantification results of ampicillin-resistant *E. coli* strain DH5α after different treatments. Data are presented as mean ± SD, n = 3. Statistically significant differences are indicated by NS (no significant difference), $*p < 0.05$, $***p < 0.001$ and $****p < 0.0001$. "+NIR" and "with NIR" mean that NIR irradiation at 1 W cm^{-2} for 12 min was employed. "#" indicates that no bacteria colonies were found on the agar plates.

that only the mannose-functionalized MoS_2 sheets precipitated in the presence of ORN178 (Figure S15, Supporting Information). The agglutination studies depicted in Figure 4i,j and Figure S16, Supporting Information, showed that L-MoS_2-Man induced fluorescent clusters greater in strength and number than those induced by S-MoS_2-Man. SEM images (Figure 4l and Figure S17a,S17b, Supporting Information) support the conclusion that L-MoS_2-Man sheets, because of their size, can bind to and almost fully cover the bacteria, forming a bacteria-sheet complex. SEM images also demonstrate that small MoS_2 sheets, while they can specifically bind to bacteria, are too small to completely cover the bacteria or form as many bacteria-sheet complexes as the large sheets do (Figure 4m and Figure S17c,S17d, Supporting Information). These findings are similar to the

previous study reported by Perreault et al., wherein large GO sheets interacted with bacteria in a cell entrapment mechanism in suspension assays.[34] Furthermore, when small and large sheets are at the same mass concentration, rather than many small sheets binding to bacteria separately and independently, a large sheet can hold bacteria more tightly because the abundant mannose residues in a single sheet make the binding more multivalent and monolithic.

We defined the agglutination index (AI) to measure and compare the ability of sheets to agglutinate bacteria according to the reported protocols. We observed significant differences between L-MoS_2-Man and other samples. The AI of L-MoS_2-Man was calculated to be 84.3, much higher than those of L-MoS_2-Glu (1.5), L-MoS_2-Gal (1.1), and S-MoS_2-Man (14.3), in accord with the above-mentioned confocal images and macroscopic results. Large mannose-functionalized MoS_2 sheets evidently possess outstanding agglutination ability for *E. coli* bacteria.

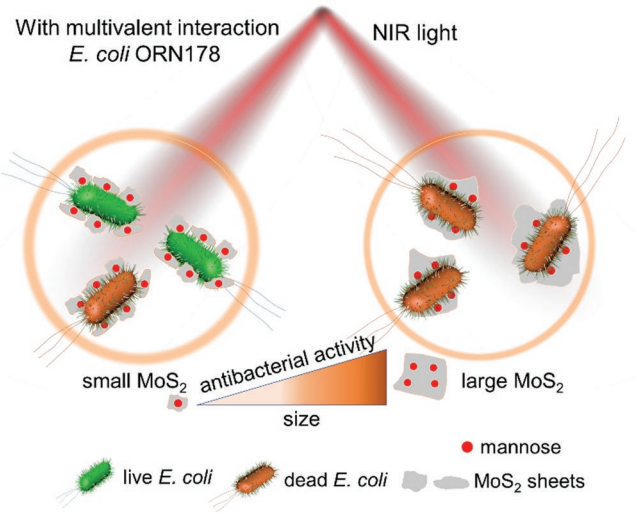

Scheme 2. Antibacterial mechanisms of different sized mannosylated MoS_2 sheets against *E. coli* ORN178.

2.4. Antibacterial Evaluations

We followed the agglutination studies by seeking to quantify the bactericidal activity intrinsic to the MoS_2 sheets' photothermal properties, applying NIR irradiation to excite the photothermal effects of MoS_2 and thus eliminate the agglutinated bacteria. To investigate the studied materials' bactericidal impact against *E. coli*, we mixed 100 µL of the materials at 1500 µg mL^{-1} with 900 µL ORN 178 or 208 bacteria solutions (10^7 CFU mL^{-1}). After incubating them for 1 h, we irradiated the suspensions for 12 min with a NIR laser at 1 W cm^{-2}. Afterwards, we spread 100 µL of solution of each sample on agar plates, then incubated the samples for 24 h to quantify the number of colonies and calculate bacterial viability (**Figure 5**). We used a PBS-treated group as a control. The bacterial viability was close to 100% in both strains treated with PBS, with or without NIR irradiation (Figure 5a–d). The lack of inhibition of bacterial growth among these PBS groups demonstrated that NIR irradiation, taken on its own, does not affect the proliferation of either bacterial strain. Meanwhile, L-MoS_2-Man significantly inhibited the growth of ORN178, and far fewer colonies were treated by L-MoS_2-Man than by S-MoS_2-Man (Figure 5a,b). These outcomes agree with an earlier finding by Perreault et al. that large sheets more potently inhibit bacterial growth, a result ascribed to their more complete entrapment of bacteria, which leads to stronger disturbance of bacterial reproduction.[34] In our case, the specific multivalent interaction between sheet and bacteria is stronger than the nonspecific entrapment seen in Perreault's studies. Under laser irradiation, both strains showed much lower bacterial viability (≈30%) when treated with L-MoS_2-OH than when incubated in PBS. As a contrast, S-MoS_2-OH showed stronger antibacterial activity in both strains owing to its better photothermal performance. As depicted in Figure 3c, the sample's temperature at 150 µg mL^{-1} increased to 61.5 °C during laser irradiation. The antibacterial ability of L-MoS_2-OH here can be attributed to bacterial death induced by its photothermal properties. Under NIR irradiation, S-MoS_2-Man exhibited distinctive bacteria elimination abilities, showing *E. coli* inhibition ratios of 89.3%. Surprisingly, we found no bacteria colony in the group treated with L-MoS_2-Man, demonstrating over 99.9% bacteria elimination efficiency. Mannosylated MoS_2 sheets can bind specifically to bacteria and form complexes, where aggregative sheets cause higher MoS_2 sheet concentrations in local areas. Therefore, mannosylated sheet suspensions can realize higher temperatures and stronger bacteria deactivation efficiency as compared to uniformly dispersed bacteria and sheets in L-MoS_2-OH suspension where no binding occurs. Because L-MoS_2-Man has much stronger agglutination abilities than S-MoS_2-Man, the groups treated with the larger sheets showed significantly lower bacterial viability than those treated with the smaller ones (**Scheme 2**). And the minimum inhibitory concentrations (MICs) of L-MoS_2-Man and S-MoS_2-Man against *E. coli* ORN178 under NIR irradiation were tested to be around 75 and 150 µg mL^{-1}, respectively.

The numbers of colonies treated by L-MoS_2-Man and S-MoS_2-Man were almost identical to control, suggesting that they have no bactericidal ability against ORN 208 (Figure 5c,d). As ORN 208 bacteria have no mannose receptors, mannosylated MoS_2 sheets do not agglutinate them, leaving them free to move about in the medium. Because L-MoS_2-Man has much stronger agglutination abilities than S-MoS_2-Man, the groups treated with the larger sheets showed significantly lower bacterial viability than those treated with the smaller ones. The stronger antibacterial effects of the small sheets can be attributed to their better photothermal performance.

In order to examine the antibacterial activities of L-MoS_2-Man against antibiotic-resistant bacteria, we used *E. coli* DH5α transfected with a pET-22b (+) plasmid as an ampicillin-resistant strain. *E. coli* DH5α is a normal *E. coli* strain with mannose receptors and becomes ampicillin-resistant upon transfection with a pET-22b (+) plasmid.[35,36] As shown in Figure 5e, only one bacteria colony remained on the agar plate after treatment with L-MoS_2-Man under NIR irradiation. Quantification results (Figure 5f) showed that L-MoS_2-Man can kill around 99.9% of bacteria in the suspension with NIR irradiation. These findings demonstrated that L-MoS_2-Man has great potential in addressing antimicrobial resistance.

2.5. Bacteria Live/Dead Assay

Having explored the agglutination abilities and antibacterial capacities of the mannose-functionalized MoS_2 sheets, we turned to a live/dead assay to evaluate their antimicrobial activity and their ability to disrupt bacterial cell membranes. Following incubation of *E. coli* ORN 178 (10^8 CFU mL^{-1}) with different materials (150 μg mL^{-1}) for 1 h, each group was exposed to NIR irradiation for 12 min (1 W cm^{-2}). The bacteria were stained with both SYTO 9 and propidium iodide (PI), and then observed by confocal microscopy (**Figure 6**a). SYTO 9 universally labels all bacteria green, whether their membranes are intact or destroyed; PI can only penetrate damaged membranes, emitting red fluorescence indicating damaged or dead bacteria. As shown in the control group, almost all bacteria were stained green by SYTO 9, suggesting that they are in "alive and active" states with an intact membrane. In the group treated with L-MoS_2-OH, few red dots were observed, and most bacteria were stained green. These results further confirmed that L-MoS_2-OH did not damage bacteria cell membranes. In sharp contrast, the L-MoS_2-OH group showed a much higher proportion (63.0%) of red fluorescence under NIR irradiation. The images revealed that the photothermal effect of MoS_2 can destroy bacteria membranes and is highly efficient in killing *E. coli* bacteria. No apparent red fluorescence was found in L-MoS_2-Man, indicating that bacterial interaction with L-MoS_2-Man suspensions does not cause bacteria inactivation. Above all, L-MoS_2-Man exhibited a predominance of dead bacteria upon NIR irradiation, with very few living bacteria visible (0.8%). The results obtained from the live/dead assay provided good agreements with the results in Figure 5, further confirming that L-MoS_2-Man with NIR irradiation showed potent antibacterial activity.

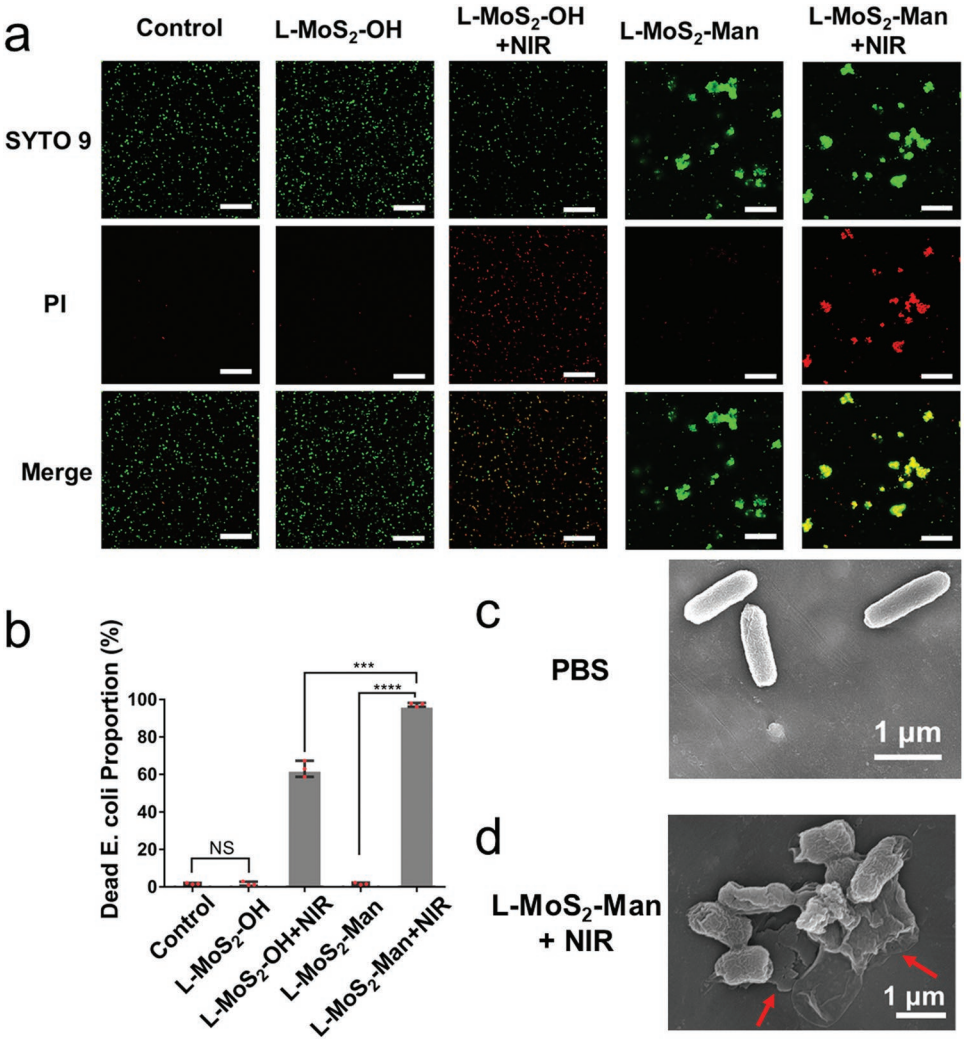

Figure 6. a) Representative confocal images of *E. coli* strain ORN 178 stained by live/dead assay after incubation with different materials. SYTO 9 (green) can stain both live and dead bacteria, while PI (red) can only stain dead bacteria. Scale bar: 20 μm. b) Biocidal activity of different samples against ORN 178, evaluated by counting bacteria or viewing fluorescence intensity from confocal images such as Figure 6a. Data are presented as mean ± SD, n = 3. Statistically significant differences are indicated by NS (no significant difference), ***$p < 0.001$ and ****$p < 0.0001$. Control group: bacteria without any treatment. SEM images of *E. coli* ORN 178 bacteria treated with c) PBS and treated with d) L-MoS_2-Man and exposed to NIR irradiation for 12 min. "+NIR" means that NIR irradiation at 1 W cm^{-2} for 12 min was employed.

To further illustrate the antibacterial mechanism of the constructed L-MoS_2-Man +NIR bactericidal system, we used SEM to check the morphological changes of the *E. coli* ORN 178 bacteria before and after treatment (Figure 6c,d). In the control group, ORN 178 had a smooth and intact surface and strong structural integrity (Figure 6c). After treatment we observed a deformed morphology, wrinkled cell surface, and in some cases complete membrane ruptures, confirming the membrane disruption mechanism (Figure 6d). BCA assays of protein contents in the supernatants after treatments confirmed the protein leakage of *E. coli* after incubation with L-MoS_2-Man under NIR irradiation (Figure S18, Supporting Information). Therefore, the effectual antibacterial performance of L-MoS_2-Man against *E. coli* most likely resulted from the specific and multivalent interactions between mannose residues on materials and FimH on the surface of ORN 178 bacteria, interactions that further led to bacteria agglutination, cell membrane destruction, and subsequent cell death.

3. Conclusions

We presented here a mild and facile synthetic approach for successfully inducing selective *E. coli* binding properties on the surface of MoS_2 sheets. Agglutination studies showed that our mannose-functionalized, water-dispersible MoS_2 sheets have a substantial affinity to *E. coli* bacteria with FimH type-1 pili, as compared to glucose- and galactose-functionalized MoS_2 sheets. The electron microscopy study revealed that bacterial binding by large mannosylated MoS_2 sheets formed a bacteria-sheet complex via multivalent interactions. Even though small MoS_2 sheets have better photothermal performance under NIR irradiation, large MoS_2 sheets prevail over them in bactericidal performance, demonstrating over 99.9% *E. coli* elimination efficiency due to their greater bacterial capture capacity. These findings have meaningful implications for future explorations of selective antibacterial properties of multivalent MoS_2 and other 2D materials. The size-dependent photothermal properties and entrapment abilities of our MoS_2 materials in suspension, along with their carbohydrate-mediated multivalent interactions, offer guidance in designing and optimizing high-performance therapeutic agents for various applications such as antimicrobials, antitumor agents, biosensors, and sewage purification.

Supporting Information

Supporting Information is available from the Wiley Online Library or from the author.

Acknowledgements

The authors acknowledge financial support by the Collaborative Research Center 765 and 1449 (431232613; sub-project B03) of the DFG and Berlin University Alliance (BUA). S.X. and X.F. acknowledge the financial support of the China Scholarship Council (CSC). S.B. acknowledges the support from DFG – Projektnummer 458564133. The authors would like to acknowledge the assistance of Dr. Kai Ludwig in TEM, Yalei Hu in AFM, and Peng Tang in SEM. Core Facility BioSupraMol is acknowledged for technical support. The authors would like to thank Ben Allen for polishing the language of this manuscript.

Open access funding enabled and organized by Projekt DEAL.

Conflict of Interest

The authors declare no conflict of interest.

Data Availability Statement

The data that support the findings of this study are available in the supplementary material of this article.

Keywords

antibacterial, mannose, MoS_2, multivalent interactions, near infrared, photothermal, polyglycerol

Received: November 25, 2021
Revised: December 16, 2021
Published online: January 30, 2022

[1] U. Theuretzbacher, K. Bush, S. Harbarth, M. Paul, J. H. Rex, E. Tacconelli, G. E. Thwaites, *Nat. Rev. Microbiol.* **2020**, *18*, 286.
[2] B. Luna, V. Trebosc, B. Lee, M. Bakowski, A. Ulhaq, J. Yan, P. Lu, J. Cheng, T. Nielsen, J. Lim, *Nat. Microbiol.* **2020**, *5*, 1134.
[3] P. Z. Kubone, K. P. Mlisana, U. Govinden, A. L. K. Abia, S. Y. Essack, *Trop. Med. Infect. Dis.* **2020**, *5*, 176.
[4] S. Larramendy, A. Gaultier, J.-P. Fournier, J. Caillon, L. Moret, F. Beaudeau, *J. Antimicrob. Chemother.* **2021**, *76*, 789.
[5] A. Gupta, S. Mumtaz, C.-H. Li, I. Hussain, V. M. Rotello, *Chem. Soc. Rev.* **2019**, *48*, 415.
[6] J. M. V. Makabenta, A. Nabawy, C.-H. Li, S. Schmidt-Malan, R. Patel, V. M. Rotello, *Nat. Rev. Microbiol.* **2021**, *19*, 23.
[7] N. Rohaizad, C. C. Mayorga-Martinez, M. Fojtů, N. M. Latiff, M. Pumera, *Chem. Soc. Rev.* **2021**, *50*, 619.
[8] R. Kurapati, K. Kostarelos, M. Prato, A. Bianco, *Adv. Mater.* **2016**, *28*, 6052.
[9] J. Hao, G. Song, T. Liu, X. Yi, K. Yang, L. Cheng, Z. Liu, *Adv. Sci.* **2017**, *4*, 1600160.
[10] K. R. Paton, J. N. Coleman, *Carbon* **2016**, *107*, 733.
[11] S. Liu, X. Pan, H. Liu, *Angew. Chem., Int. Ed. Engl.* **2020**, *132*, 5943.
[12] C. B. He, Y. P. Hu, L. C. Yin, C. Tang, C. H. Yin, *Biomaterials* **2010**, *31*, 3657.
[13] W. Jiang, B. Y. S. Kim, J. T. Rutka, W. C. W. Chan, *Nat. Nanotechnol.* **2008**, *3*, 145.
[14] D. A. Canelas, K. P. Herlihy, J. M. DeSimone, *Wiley Interdiscip. Rev.: Nanomed. Nanobiotechnol.* **2009**, *1*, 391.
[15] X. J. Zhang, Z. M. Zhang, S. Y. Zhang, D. Y. Li, W. Ma, C. X. Ma, F. C. Wu, Q. Zhao, Q. F. Yan, B. S. Xing, *Small* **2017**, *13*, 1701210.
[16] K. Yang, J. Wan, S. Zhang, B. Tian, Y. Zhang, Z. Liu, *Biomaterials* **2012**, *33*, 2206.
[17] Z. Chen, C. Yu, I. A. Khan, Y. Tang, S. Liu, M. Yang, *Ecotoxicol. Environ. Saf.* **2020**, *197*, 110608.
[18] Q. Gao, X. Zhang, W. Yin, D. Ma, C. Xie, L. Zheng, X. Dong, L. Mei, J. Yu, C. Wang, *Small* **2018**, *14*, 1802290.
[19] M. Li, L. Li, K. Su, X. Liu, T. Zhang, Y. Liang, D. Jing, X. Yang, D. Zheng, Z. Cui, *Adv. Sci.* **2019**, *6*, 1900599.
[20] X. Zhang, G. Zhang, H. Zhang, X. Liu, J. Shi, H. Shi, X. Yao, P. K. Chu, X. Zhang, *Chem. Eng. J.* **2020**, *382*, 122849.

[21] Y. Chen, Q. Ji, G. Zhang, H. Liu, J. Qu, *Angew. Chem., Int. Ed. Engl.* **2021**, *133*, 7823.
[22] P. Jain, C. D. Shanthamurthy, P. M. Chaudhary, R. Kikkeri, *Chem. Sci.* **2021**, *12*, 4021.
[23] A. Pancaro, P. Georgiou, A. N. Baker, M. Walker, P. Adriaensens, M. I. Gibson, I. Nelissen, *Nanoscale* **2021**, *13*, 10837.
[24] S. Bhatia, M. Dimde, R. Haag, *MedChemComm* **2014**, *5*, 862.
[25] S. Bhatia, L. C. Camacho, R. Haag, *J. Am. Chem. Soc.* **2016**, *138*, 8654.
[26] M. Scalabrini, J. Hamon, I. Linossier, V. Ferrières, K. Réhel, *Colloids Surf., B* **2019**, *183*, 110383.
[27] X. Chen, N. C. Berner, C. Backes, G. S. Duesberg, A. R. McDonald, *Angew. Chem., Int. Ed. Engl.* **2016**, *55*, 5897.
[28] T. Liu, C. Wang, X. Gu, H. Gong, L. Cheng, X. Shi, L. Feng, B. Sun, Z. Liu, *Adv. Mater.* **2014**, *26*, 3433.
[29] S. Wang, K. Li, Y. Chen, H. Chen, M. Ma, J. Feng, Q. Zhao, J. Shi, *Biomaterials* **2015**, *39*, 206.
[30] Y. Zhang, G. Jia, P. Wang, Q. Zhang, X. Wei, E. Dong, J. Yao, *Superlattices Microstruct.* **2017**, *105*, 22.
[31] D.-W. Lee, T. Kim, I.-S. Park, Z. Huang, M. Lee, *J. Am. Chem. Soc.* **2012**, *134*, 14722.
[32] G. Yu, Y. Ma, C. Han, Y. Yao, G. Tang, Z. Mao, C. Gao, F. Huang, *J. Am. Chem. Soc.* **2013**, *135*, 10310.
[33] B. Schmidt, S. Sankaran, L. Stegemann, C. A. Strassert, P. Jonkheijm, J. Voskuhl, *J. Mater. Chem. B* **2016**, *4*, 4732.
[34] F. Perreault, A. F. De Faria, S. Nejati, M. Elimelech, *ACS Nano* **2015**, *9*, 7226.
[35] H. Y. Yang, H. F. Zhou, H. Y. Hao, Q. J. Gong, K. Nie, *Sens. Actuators, B* **2016**, *229*, 297.
[36] Y. Luo, Y. Gu, R. Feng, J. Brash, A. M. Eissa, D. M. Haddleton, G. Chen, H. Chen, *Chem. Sci.* **2019**, *10*, 5251.